A Residential Miniboost Photovoltaic Inverter with Maximum Power Point Operation and Power Quality Compensation

Zeng Xiang, *Member*, *IEEE*, Ying Pang, *Student Member*, *IEEE*, Ziyi Bai, Lei Wang, *Senior Member*, Chi-Kong Wong, *Member*, *IEEE*, Wai-Hei Choi, *Member*, *IEEE*, Chi-Seng Lam, *Senior Member*, *IEEE*, and Man-Chung Wong, *Senior Member*, *IEEE*

Abstract **– Among the exiting multifunctional photovoltaic (PV) inverters (MPVIs), the main challenges are low efficiency, undesired harmonic emission, and weak compensation capability. In this paper, a theoretical study via rotating phasor to the PV curves is firstly proposed to figure out the undesired harmonic emission puzzle in different PV inverters as well as to provide the foundation for PV inverters to achieve multifunction ability under varying load conditions. On the other hand, a single-phase time-sharing miniboost MPVI with different operation modes is proposed and operated under varying PV and load conditions in order to improve its efficiency and compensation capability without undesired harmonic emission. Corresponding control strategy and stability analysis are given. Finally, a 1.5-kW prototype is presented, benchmarked against harmonic emission issues, compensation capability, and efficiency. Experimental results clearly indicate that the proposed topology and control method can perform the active power injection and power quality compensation with better efficiency and avoiding harmonic emission into the grid dynamically.**

Index Terms **– Multifunctional photovoltaic inverter, power quality, photovoltaic generation system.**

Manuscript received March 11, 2022; revised May 30, 2022; accepted June 20, 2022. This work was supported in part by the Macau Science and Technology Fund, Macau SAR, under Project FDCT 0026/2019/A1, in part by the State Key Laboratory of Internet of Things for Smart Cities of University of Macau under Project SKL-IOTSC(UM)-2021-2023, in part by the Guangdong-Hong Kong-Macau Joint Laboratory for Smart Cities under Project EF008/IOTSC-YKV/2021/GDSTC, in part by the State Key Laboratory of Analog and Mixed-Signal VLSI of University of Macau under Project SKL-AMSV(UM)-2021-2023, in part by the National Natural Science Foundation of China under Project 52107191, and in part by Hunan Youth Science and Technology Innovation Talents Program under Project 2021RC3059. (Corresponding author: Lei Wang; Ying Pang).

Zeng Xiang, Ying Pang, Ziyi Bai, Chi-Kong Wong, and Wai-Hei Choi are with the State Key Laboratory of Internet of Things for Smart City, University of Macau, Macao 999078, China, also with the Department of Electrical and Computer Engineering, Faculty of Science and Technology, University of Macau, Macao 999078, China (e-mail: yb57435@umac.mo; yb87446@um.edu.mo; yc07909@um.edu.mo; ckwong@um.edu.mo; Heichoi@um.edu.mo).

Lei Wang is with the College of Electrical and Information Engineering, Hunan University, Changsha 410000, China (email: jordanwanglei@hnu.edu.cn).

Chi-Seng Lam is with the State Key Laboratory of Analog and Mixed-Signal VLSI, University of Macau, Macao 999078, China, also with the Institute of Microelectronics, University of Macau, Macao 999078, China, and also with the Department of Electrical and Computer Engineering, Faculty of Science and Technology, University of Macau, Macao 999078, China (e-mail: cslam@um.edu.mo).

Man-Chung Wong is with the State Key Laboratory of Internet of Things for Smart City, University of Macau, Macao 999078, China, and also with the State Key Laboratory of Analog and Mixed-Signal VLSI, University of Macau, Macao 999078, China, and also with the Department of Electrical and Computer Engineering, Faculty of Science and Technology, University of Macau, Macao 999078, China (e-mail: mcwong@umac.mo).

I. Introduction

The penetration level of distributed energy resources (DERs) systems is increasing since it is an effective solution to carbon neutrality [1]. On the one hand, the DERs are increasingly essential parts of the smart grid or energy internet. On the other hand, due to the numerous power electronic interfaces of DERs, such as the rooftop photovoltaic (PV) systems and the local residential loads, the power quality issues have become severe. The power quality issues affect the stability and efficiency of the residential power system operation. To cope with these issues, some extra passive and/or active devices are recommended to add. To make efficient use of DERs and to fulfill standard power quality requirements, multifunctional photovoltaic inverters (MPVIs) are considered as more cost-effective solutions since the PV inverters (PVIs) have similar circuit topologies as power quality conditioners. With the aid of MPVIs, extra power quality conditioners may no longer be essential. Thus, the additional space, investment, and operational cost of power quality conditioners are avoided.

The MPVIs have attracted the attention of many researchers due to these benefits. Some MPVIs such as typical single-stage and two-stage topologies, can meet residential multifunctional application requirements, but some challenges need to be overcome [2]. On the one hand, the operation of 41% of the rooftop PV systems had been affected by shading, with energy losses about 10% in [3]. On the other hand, the dc voltage rating of these MPVIs is high resulting in high cost and operational losses. Also, the determination of the dc voltage rating is seldom discussed quantitatively and theoretically for these MPVIs. Among the existing literature [4]−[7], some puzzles are listed as follows.

- Maximum power point tracking (MPPT) always adjusts the dc voltage quickly, so interharmonics are introduced into the power grid as [4];
- Power quality function can be improved in MPVIs with varying dc voltage in [5];
- Partial harmonic current compensation in multifunctional PV inverter should be performed when the inverter capacity is not enough as [6];
- Time-varying interharmonics in different types of grid-tied PV inverter systems exist in [7].

A corresponding topology and control strategy should be developed to handle the above-mentioned challenges.

The pseudo-dc [8], [9], quasi-single-stage [10]- [12], and time-sharing [13], [14] topologies have achieved good performances. Except for the topology in [12], other topologies have no compensation data or cannot act as a compensator due

TABLE I
COMPARISON OF EXISTING TOPOLOGIES

Topologies	Proposed year	Source Voltage (Line-Line)	DC voltage * (Ratio of dc voltage to source RMS voltage)	No. of components			Functions			Efficiency (%)		Cost-effectiveness
				IGBT	Diode	Trans-former	Active power injection	Reactive power comp.	Harmonic comp.	PG mode*	MF mode*	
[8], [9]	2013, 2014	Single-phase 220 V	NA **	5	6	1	Yes	NA	NA	87	NA	Low
[10]	2018	Single-phase 56 V	100V (1.7)	9	10	0	Yes	NA	NA	93.7	NA	Low
[11], [12]	2019, 2020	Three-phase 400 V	700V (1.7)	13	14	0	Yes	Yes	Yes	95.2	86.4	Low
[13], [14]	2004, 2017	Three-phase 400 V	650V (1.6)	14	18	0	Yes	NA	NA	92.4	NA	Medium
This paper	2022	Single-phase 115 V	162V (1.4)	5	6	0	Yes	Yes	Yes	94.4	91.4	High

*Note: NA stands for Not Available; * stands for the lowest value from the operational range; ** DC capacitor of the converter is replaced by a dedicated circuit, so that the dc voltage and ratio are not available; PG stands for power generation, which contains only active power injection; MF stands for multifunction, which contains active power injection, reactive power, or/and harmonic current compensation simultaneously.*

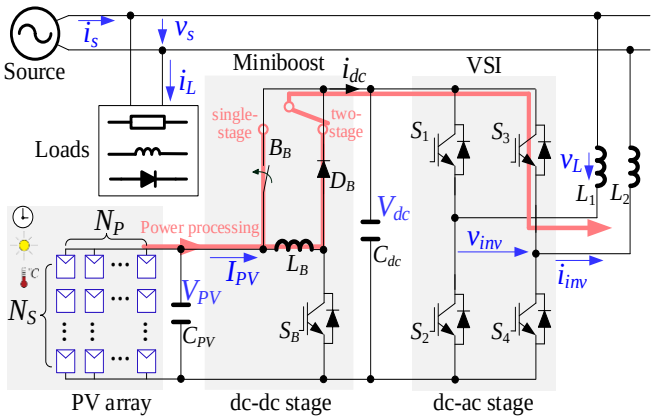

Fig. 1. Circuit configuration of the proposed MPVI.

to the elimination of the dc capacitor in [9]. However, the voltage stress of the power semiconductor is high in [12] since the dc voltage of the upper and lower capacitor are unbalanced. As a result, higher voltage level power semiconductors are required, which leads to high cost. The discussions are summarized in TABLE I, in which a ratio of dc voltage to source RMS voltage is given. The lower ratio means the operating dc voltage of the inverter is lower. Then, the lower ratio indicates the lower cost of inverter. The pseudo-dc topology needs additional transformer resulting in high cost and low efficiency. Compared with a common single-phase H-bridge, the number of components is larger, resulting in high cost and low cost-effectiveness [10]. The time-sharing miniboost topologies with single- and two-stage modes in [13][14] have better performance except for the compensation function. The miniboost is only engaged (in two-stage mode) to transport partial power when the maximum power point (MPP) voltage is low. At other times, the miniboost is bypassed (in single-stage). The miniboost does not always operate, and its capacity is relatively small compared to the standard boost converter resulting in medium cost-effectiveness. But it selects 1.6 times source voltage as the fixed transfer threshold between the single- and two-stage mode, which increases the operational losses. Therefore, some challenges (including compensation capacity, efficiency, and harmonic emission puzzles) must be addressed when the time-sharing miniboost topology is considered for multifunctional applications. The contributions of this paper are listed as follows.

1) A graphical analysis method is proposed, which can be applied to exiting PV inverters for active power injection and/or power quality compensation under varying PV and load conditions. The proposed analysis method rotates phasor to PV curves to figure out the puzzle of undesired harmonic emission and formulate operational criteria;

2) A time-sharing miniboost MPVI is proposed to eliminate undesired harmonic and improve compensation performance by engaging miniboost adaptively for MPP operation and power quality compensation simultaneously;

3) The proposed MPVI can harvest maximum solar energy and perform full compensation without undesired harmonic emission under varying PV and load conditions.

Based on the above contributions and corresponding experimental results in Section V, the following results can be obtained:

- The PV inverter [17] that operates at MPP will induce undesired harmonics with THD=27.6%. After using the proposed approach, the PV inverter can not only achieve MPP operation but also eliminate undesired harmonics with THD=2.5% in TABLE IV;
- Under the marginal MPP voltage situation, the PV inverter may choose either MPP operation or full compensation operation. With MPP operation, the source power factor (PF_S) is 0.24 (Fig. 16 case in Table V). With full compensation operation (PF_S= 1), the extracted solar energy is less than 5.3% (Fig. 17 case) than that of MPP operation. After using the proposed approach, maximum solar energy can be extracted with full compensation (Fig. 18 case in Table V);
- Under varying PV conditions, the proposed approach can perform MPP operation and full compensation with 1.1~2.5% better efficiency, as shown in Tables VI, V, and IV.

The rest of this paper is layout as follows. Section II presents the circuit configuration, power processing modes, and efficiency of the proposed MPVI. The graphical analysis is presented in Section III. The control algorithm is proposed in Section IV. The experimental results are presented in Section V. Finally, the conclusions are drawn in Section VI.

II. TOPOLOGY CHARACTERISTICS AND EFFICIENCY

The proposed MPVI is depicted in Fig. 1, which consists of an H-bridge voltage source inverter (VSI), a miniboost, and a bypass breaker (B_B). The v_s and i_s are the source voltage and current, respectively. The v_{inv} and i_{inv} are the inverter output voltage and current, respectively. The v_L is the voltage across coupling inductor L (L=L_1+L_2). The V_{PV} and I_{PV} are the PV array voltage and current, respectively. The V_{dc} is the dc voltage of the inverter.

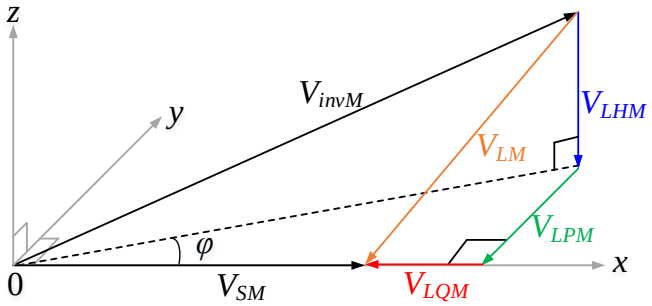

Fig. 3. Inverter voltage in a 3-dimensional view.

A. *Power Processing Modes (Single- or Two-Stage)*

The topology is designed to operate in single- or two-stage modes adaptively. In single-stage mode, whether PV array is connected to the inverter dc side, the single-stage mode can be subdivided into single-stage PV-connected and single-stage inverter alone modes. The single-stage inverter alone mode is mainly suitable for the condition of no solar energy in the PV array (at night).

For single-stage PV-connected mode, the B_B is ON, and S_B is OFF. The miniboost is bypassed. Thus, the V_{PV} and V_{dc} are in parallel and equal. The V_{inv} can be expressed as:

$$V_{invM} = m \cdot V_{dc} = m \cdot V_{PV} \tag{1}$$

where m is the index of pulse width modulation (PWM).

In two-stage mode, the miniboost is engaged by turning B_B OFF. Due to the decoupling effect of miniboost, V_{PV} is different from V_{dc}. The inverter voltage can be expressed as:

$$V_{invM} = m \cdot V_{dc} = m \cdot \frac{V_{PV}}{1\text{-}d} \tag{2}$$

where d is the duty ratio of miniboost.

B. *Efficiency*

The operational losses mainly contain two types, namely, MPPT extraction losses and conversion losses [15], [16]. The MPPT efficiency η_{MPPT} can represent extraction losses as:

$$\eta_{MPPT} = \frac{V_{PV} \cdot I_{PV}}{V_{MPP} \cdot I_{MPP}} \tag{3}$$

where the $V_{PV} \cdot I_{PV}$ means the extracted power by the MPPT algorithm. The $V_{MPP} \cdot I_{MPP}$ is the theoretical maximum power of the PV array. The conversion losses contain dc-dc (p_{dc_Loss}) and dc-ac (p_{ac_Loss}) power losses. Therefore, the operational efficiency can be expressed as:

$$\eta = \eta_{MPPT} \cdot \frac{v_{inv} \cdot v_{inv}}{v_{inv} \cdot v_{inv} + (1 - B_B)\, p_{dc\_Loss} + p_{ac\_Loss}} \tag{4}$$

where B_B= 1 if the B_B is ON. Otherwise, B_B= 0. In general, the MPPT efficiency of the two-stage mode is higher [17]. However, the extra dc-dc conversion losses are introduced (B_B = 0). The appropriate power processing stage selected criteria are discussed in the next section.

III. Proposed Graphical Analysis and Operational Criteria

In this section, a graphical analysis between the phasor and PV curve is proposed to figure out the puzzle of the undesired harmonic emission and weak compensation capability. Based on the graphical analysis, different possible operational criteria are presented under varying conditions.

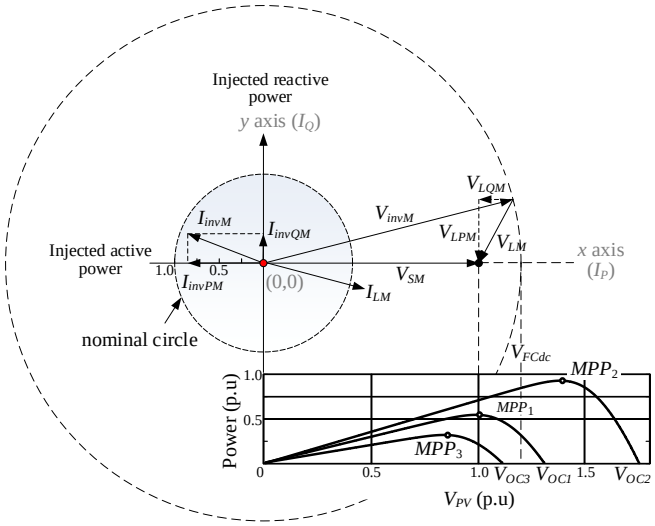

Fig. 2. Phasor diagram and *P-V* curves combination example.

A. *Proposed Graphical Analysis*

In Fig. 3, the subscript M means magnitude value, V_{LPM}, V_{LQM}, and V_{LHM} are magnitudes of the active, reactive, and harmonic components of the voltage across the inductor V_{LM}, respectively [18]. The x-axis is the reference for source voltage V_{SM}. The inverter reactive current I_{invQM} is leading the V_{SM} by π/2, and the V_{LQM} is leading the I_{invQM} by π/2 (inductive impedance), so the V_{LQM} is also on the x-axis. Similarly, the y-axis and z-axis are indicated to inject active and harmonic currents into the grid by the inverter, respectively. According to the geometric relationship in Fig. 3, the magnitude of inverter voltage V_{invM} can be expressed as:

$$\begin{aligned} V_{invM} &= \sqrt{\left(V_{SM} + V_{LQM}\right)^2 + V_{LPM}^2 + V_{LHM}^2} \\ &= \sqrt{\left(V_{SM} + X_L \cdot I_{invQM}\right)^2 + X_L^2 \cdot I_{invPM}^2 + \sum_{n=2}^{\infty} h^2 X_L^2 I_{invnM}^2} \end{aligned} \tag{5}$$

where X_L is the fundamental frequency (f_1) impedance of the inductor and equals to $2\pi f_1 L$. The I_{invPM}, and I_{invnM} are magnitudes of fundamental active and harmonics current components of the inverter current, respectively.

When $V_{LHM} \neq 0$, the z-axis should be considered, which points out of the paper in a 3-dimensional view. For concise analysis, the harmonic component is ignored, i.e., V_{LHM}=0. The simplified 2-dimensional phasor diagram and the power-voltage (*P-V*) curve are plotted in Fig. 2:

1) The varying PV conditions (including irradiance, temperature, shading variation, etc.) lead to varying MPP (V_{MPP}, P_{MPP}) and inverter active power current I_{invPM}.

2) The I_{LM} is the varying load current. The proposed MPVI injects varying reactive current I_{invQM} to compensate load reactive current. The reactive voltage across the coupling inductor V_{LQM} is on the x-axis.

3) The rotated V_{invM} on the x-axis is defined as V_{FCdc} to perform graphical analysis. The dc voltage is benchmarked with V_{SM}. The V_{PV} is equal to 1.0 when $V_{PV} = V_{SM}$.

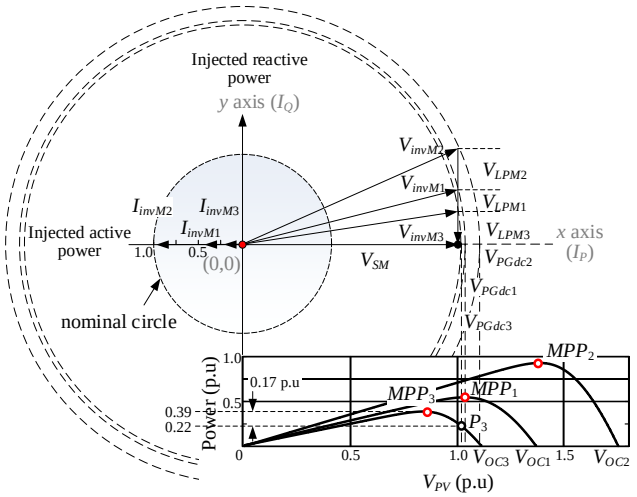

Fig. 4. Phasor diagram and *P-V* curves under active power injection (PG mode).

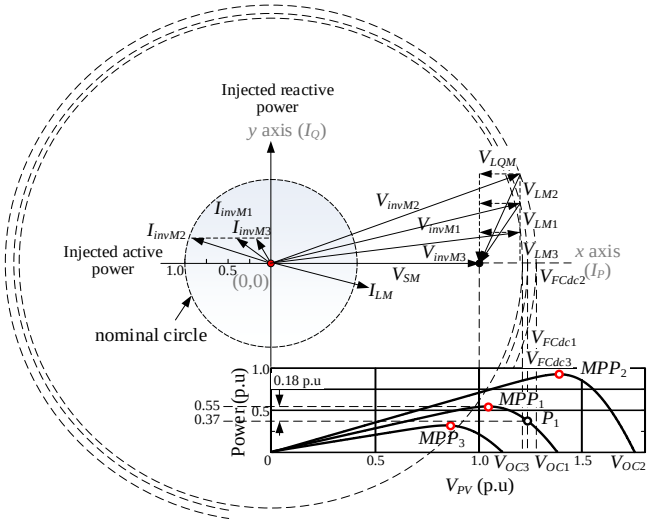

Fig. 5. Phasor diagram and *P-V* curves under active power injection and reactive power compensation (MF mode).

4) $I_{invM}=\sqrt{I_{invPM}^2+I_{invQM}^2+I_{invHM}^2}$ should be limited by the nominal current for safe operation.

Based on the above discussions, power generation (PG), multifunctional (MF), and compensation operation modes (CM) are presented as follows.

B. *Power Generation Mode*

In PG Mode, only active power injection is considered. The conversion losses are ignored for simplicity so that the solar energy of the PV array is equal to the injected active power to the grid ($V_{PV}\cdot I_{PV}=V_S\cdot I_{invP}$). Therefore, the magnitude of the active power current of the inverter can be deduced as:

$$I_{invPM}=\frac{P_{PV}}{V_{SM}}. \tag{6}$$

The corresponding magnitude of inverter voltage can be deduced as:

$$V_{invM}=\sqrt{V_{SM}^2+X_L^2 I_{invPM}^2}. \tag{7}$$

Substituting (7) into (1), when m is equal to 1, the $V_{PGdc}=V_{invM}$ expresses the required minimum dc voltage of the inverter to inject active power current I_{invPM} into the grid. According to the relationship between V_{PGdc} and MPP voltage V_{MPP}, the PG mode can be subdivided into three different type cases such as marginal, high, and low MPP voltage cases.

1) *Marginal MPP Voltage (MPP_1)*

In this case, the V_{PGdc1} is equal to MPP voltage V_{MPP1}, as shown in Fig. 4, which is the marginal/critical situation. It should be noted that the V_{PGdc1} is not the projection of V_{invM1} on the x-axis, but the length of V_{invM1} rotated on the x-axis. Under the marginal situation, the VSI operates at MPP. The MPP voltage is marginal to inject MPP power into the grid with the sinusoidal current. The related experimental result is given in Fig. 15 in Section V.B.

From another point of view, the V_{invM1} maybe increase to be larger such as V_{invM2} in Fig. 4. The clockwise rotated V_{invM2} magnitude on the x-axis shows that $V_{invM2}=V_{PGdc2}>V_{MPP1}$. Under this situation, the inverter falls to the overmodulation region (substituting V_{invM2} and V_{MPP1} into (1), m>1), which causes undesired harmonic emission [19]. Therefore, the injected current must be decreased. When the injected current is decreased to V_{invM1}, the VSI turns back to MPP operation. Conversely, the decreased V_{invM1} to V_{invM3} is shown in Fig. 4. As a result, the clockwise rotated V_{invM3} magnitude on the x-axis shows that $V_{invM3}=V_{PGdc3}<V_{MPP1}$. Under this situation, the VSI should be controlled to operate at MPP_1 to release maximum power into the grid.

2) *High MPP Voltage (MPP_2)*

In this case, the MPP voltage V_{MPP2} is larger than the required dc voltage V_{PGdc2} as shown in Fig. 4. As discussed in section III B.1), the inverter should be operated at MPP_2 to inject maximum power into the grid. The single-stage PV-connected mode is selected by adjusting the modulation index. This case is similar to high MPP voltage in multifunction mode as discussed in section III C.2).

3) *Low MPP Voltage (MPP_3)*

In this case, the MPP voltage V_{MPP3} is less than the required dc voltage V_{PGdc3} as shown in Fig. 4. The inverter can extract 0.22 p.u solar energy at P_3 ($V_{P3}=V_{PGdc3}$) instead of 0.39 p.u at MPP_3.

Under this situation, the proposed MPVI can operate at P_3 (single-stage PV-connected mode) or MPP_3 (two-stage mode). When the proposed MPVI operates at MPP_3, dc-dc losses are activated despite extracting 0.39 p.u solar energy. If the dc-dc stage losses are lower than extraction losses (0.39 - 0.22 p.u), the two-stage mode is preferred.

Representative experimental cases are studied and given in Fig. 11, Fig. 12, and Fig. 13 in Section V.A and TABLE IV. In Fig. 11, the inverter operates at MPP in single-stage PV-connected mode. But the inverter current is distorted since the inverter with low MPP voltage falls to overmodulation region.

In Fig. 12, the inverter operates deviating from MPP (similar to P_3 in Fig. 4) in single-stage PV-connected mode. The VSI current is sinusoidal, but less solar energy can be extracted than that of Fig. 11. In Fig. 13, the inverter operates at MPP_3 in two-stage mode, the inverter current is sinusoidal, and the efficiency is higher. Therefore, the two-stage mode is preferred under this situation as more active power can be injected.

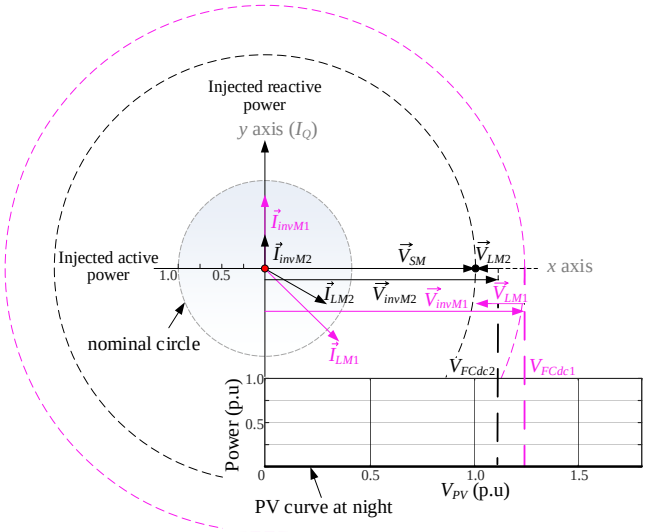

Fig. 6. Phasor diagram in compensation mode (CM mode).

C. Multifunction Mode

The inverter injects active power, reactive power, and harmonic current in multifunction mode. Referring to (5), ignoring harmonic component, (8) can be obtained.

$$V_{invM} = \sqrt{\left(V_{SM} + X_L \cdot I_{invQM}\right)^2 + X_L^2 \cdot I_{invPM}^2} \ . \tag{8}$$

Substituting (8) into (1), when m is equal to 1, the V_{FCdc} expresses the required minimum dc voltage for maximum power injection and full compensation. It should be noted that the voltage formed by the reactive current flowing through the coupling inductor is in phase with source voltage V_{SM}. As a result, the V_{FCdc} is larger than V_{SM}. The multifunction mode can be analyzed through Fig. 5 under marginal, high, and low MPP voltage cases such as MPP_1, MPP_2, and MPP_3, respectively.

1) *Marginal MPP Voltage (MPP_1)*

In this case, the proposed MPVI can operate in single- or two-stage mode, as discussed below.

In single-stage mode, only VSI operates, so the flexibility of the control strategy is limited. In Fig. 5, the MPP_1 voltage can meet the requirement of injected active power (as discussed in section III. B.1)) but not meet the reactive current requirement ($V_{MPP1}<V_{FCdc1}$). As a result, there are two possible approaches, such as VSI operates 1) at P_1, 2) at MPP_1. At P_1, VSI can compensate reactive current, but the extracted solar energy is not maximum. At MPP_1, VSI extracts maximum solar energy but only performs partial compensation. The maximum active power injection is preferred from the viewpoint of harvesting more solar energy. However, if the power quality does not meet the local grid code, implementing power quality enhancement is the priority. Then, active power injection is the second consideration.

In two-stage mode, the B_B is OFF to engage the miniboost. The miniboost performs MPPT and the inverter performs full compensation by adjusting the modulation index to regulate V_{dc} to V_{FCdc1}. The related experimental result will be given in Fig. 15, Fig. 16, Fig. 17, and Fig. 18 in section V.B.

In single-stage mode, the proposed MPVI with marginal MPP voltage can inject maximum active power as shown in Fig. 15. Under this situation, only partial reactive power can be compensated, as shown in Fig. 16. The proposed MPVI operates with MPP as shown in Fig. 17, less solar energy can be extracted. But full compensation can be performed.

In the two-stage mode, the VSI performs full compensation as shown in Fig. 18 and TABLE V. More active power is injected and reactive power is fully compensated. Therefore, the two-stage mode is preferred.

2) *High MPP Voltage (MPP_2)*

Referring to (8) and Fig. 5, the clockwise rotated V_{invM2} on the x-axis is less than V_{MPP2}. Therefore, the VSI can operates at MPP_2 for full reactive power compensation in the single-stage PV-connected mode. Although the proposed MPVI can operate in the two-stage mode to perform MPPT and full compensation, the power losses are larger. That's because the PV current flows through the inductor L_B and diode D_B in two-stage mode (without B_B or B_B OFF). The internal resistance of the inductor (the winding of the inductor is relatively long) and diode D_B introduce conduction losses. When the proposed MPVI operates in single-stage PV-connected mode (B_B ON), the PV current flows through B_B since the internal resistance of B_B is much smaller than that of L_B and diode D_B. As a result, the power losses are less. Fig. 19 and Fig. 20 show that the proposed MPVI operates in single-stage and two-stage mode, respectively. TABLE VI shows the single-stage mode is preferred with higher efficiency.

3) *Low MPP Voltage (MPP_3)*

In this case, the MPP voltage is V_{MPP3}. The clockwise rotated V_{invM3} on the x-axis is V_{FCdc3}, larger than V_{MPP3}, as shown in Fig. 5. The two-stage mode should be selected to avoid harmonic emission. In two-stage mode, the miniboost is operated at MPP3, and VSI is operated at V_{FCdc} for full compensation. The related experimental result is given in Fig. 14 in Section V.A and TABLE IV. The dc voltage of the MF mode is regulated higher than that of the PG mode in Fig. 13 due to reactive power increase.

TABLE II
PROPOSED MPVI OPERATIONAL CRITERIA UNDER VARYING CONDITIONS

	Function	Section and PV voltage situation	Voltage condition	Operation mode		B_B	Miniboost	PV voltage	DC voltage
Day	Active power generation (PG)	III.B.1 Marginal MPP voltage and III.B.2 High MPP voltage	$V_{SM} \le V_{MPP}$	Single-stage PV-connected mode		ON	Bypass	V_{MPP}	V_{MPP}
Day	Active power generation (PG)	III.B.3 Low MPP voltage	$V_{MPP} < V_{SM}$	Higher efficiency one between	Single-stage PV-connected mode	ON	Bypass	V_{PGdc}	$V_{PGdc}>V_{SM}$
					Two-stage mode	OFF	Engage	V_{MPP}	$V_{PGdc}>V_{SM}$
Day	Multifunction (MF)	III.C.1 Marginal MPP voltage	$V_{SM} \approx V_{MPP} < V_{FCdc}$	Two-stage mode		OFF	Engage	V_{MPP}	$V_{FCdc}>V_{SM}$
Day	Multifunction (MF)	III.C.2 High MPP voltage	$V_{FCdc} < V_{MPP}$	Single-stage PV-connected mode		ON	Bypass	V_{MPP}	V_{MPP}
Day	Multifunction (MF)	III.C.3 Low MPP voltage	$V_{MPP} < V_{SM} < V_{FCdc}$	Two-stage mode		OFF	Engage	V_{MPP}	V_{FCdc}
Night	Compensation Only	III.D	$V_{FCdc} > V_{SM}$	Single-stage inverter alone mode		OFF	Bypass		V_{FCdc}

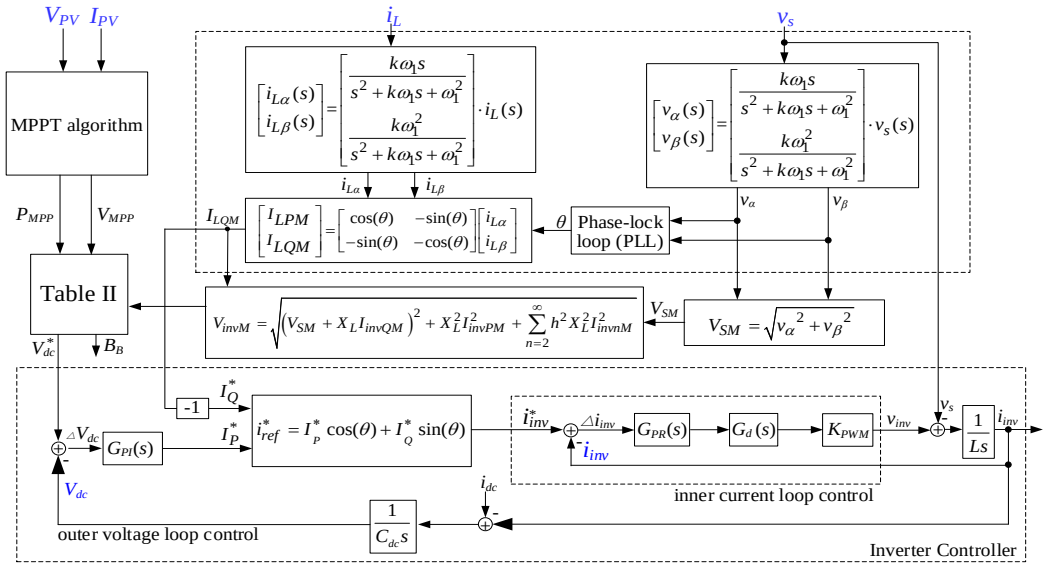

Fig. 7. Control block diagram of the proposed MPVI.

D. Compensation Mode

At night, PV array have no solar energy injected into the power grid. Only reactive power is needed to be compensated. Under this situation, the required inverter ac voltage V_{invM} can be expressed as:

$$V_{invM}=\sqrt{\left(V_{SM}+X_L\cdot I_{invQM}\right)^2}=V_{SM}+X_L\cdot I_{invQM}\,. \tag{9}$$

Fig. 6 shows the phase diagram in compensation mode. Comparing V_{invM1} and V_{invM2} shows that injecting a higher reactive current requires higher ac voltage. According to (1), the larger reactive power requires a larger dc voltage. The related experimental result will be given in Fig. 21, in which the harmonic current is also compensated.

Based on the above analysis, the operational criteria are summarized in TABLE II under varying conditions.

IV. Control Algorithm and Stability Analysis

A. Control Algorithm

In this section, the algorithm of detecting load reactive power current I_{LQM}, source voltage V_{SM} and MPP (V_{MPP}, P_{MMP}) of the PV array are presented. The inverter injected opposite reactive power ($-I_{LQM}$) to perform full compensation. According to I_p-I_q algorithm [20], the load reactive current I_{LQM} can be obtained as:

$$\begin{bmatrix} I_{LPM} \\ I_{LQM} \end{bmatrix}=\begin{bmatrix} \cos(\theta) & -\sin(\theta) \\ -\sin(\theta) & -\cos(\theta) \end{bmatrix}\begin{bmatrix} i_{L\alpha} \\ i_{L\beta} \end{bmatrix} \tag{10}$$

where θ is the voltage phase angle given by the phase-locked loop (PLL). The $i_{L\alpha}$ and $i_{L\beta}$ are the load currents in the $\alpha\beta$ reference frame, which can be obtained by orthogonal generation methods (OGMs). The second-order generalized integrator (SOGI) method [21] is selected in this paper, and $i_{L\alpha}$ and $i_{L\beta}$ can be expressed as:

$$\begin{bmatrix} i_{L\alpha}(s) \\ i_{L\beta}(s) \end{bmatrix}=\begin{bmatrix} G_\alpha(s) \\ G_\beta(s) \end{bmatrix}\cdot i_L(s) \tag{11}$$

where $G_\alpha(s)$ and $G_\beta(s)$ can be expressed as:

$$G_\alpha(s)=\frac{k\omega_1 s}{s^2+k\omega_1 s+\omega_1^2} \tag{12}$$

$$G_\beta(s)=\frac{k\omega_1^2}{s^2+k\omega_1 s+\omega_1^2} \tag{13}$$

where k is the damping coefficient, ω_1 is the fundamental angular frequency. The magnitude of source voltage can be calculated in the $\alpha\beta$ reference frame by:

$$V_{SM}=\sqrt{v_\alpha^2+v_\beta^2} \tag{14}$$

where the v_α and v_β are the source voltage in the αβ reference frame. Similarly, v_α and v_β can be obtained by:

$$\begin{bmatrix} v_\alpha(s) \\ v_\beta(s) \end{bmatrix}=\begin{bmatrix} G_\alpha(s) \\ G_\beta(s) \end{bmatrix}\cdot v_s(s)\,. \tag{15}$$

The MPP (V_{MPP}, P_{MPP}) can be detected by the improved perturb and observe (P&O) MPPT algorithm [22]. So far, the necessary conditions in TABLE II for selecting power processing stage are presented.

Based on the above analysis, the control strategy is summarized in Fig. 7, in which the dc voltage control adopts proportional-integral (PI) controller presented as:

$$G_{PI}(s)=K_{PI}+\frac{K_I}{s} \tag{16}$$

where K_{PI} and K_I are proportional coefficient and integral coefficient, respectively. The proportional resonant (PR) controller is employed to track the output current with zero steady-state error in the current control module. The PR controller is expressed as:

$$G_{PR}(s)=K_{PR}+K_R\frac{2\cdot\omega_C\cdot s}{s^2+2\cdot\omega_C\cdot s+\omega_1^2} \tag{17}$$

where K_{PR}, K_R and ω_C are proportional coefficient, resonant gain, and cut-off frequency, respectively.

B. Stability Analysis

According to the current inner loop in Fig. 7, the open-loop transfer function can be written as:

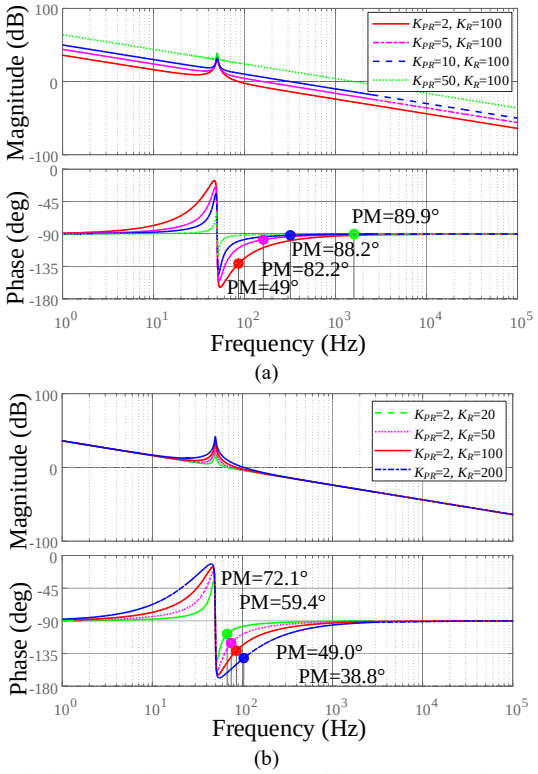

Fig. 8. Bode diagram with varying (a) K_{PR} and (b) K_R in current loop.

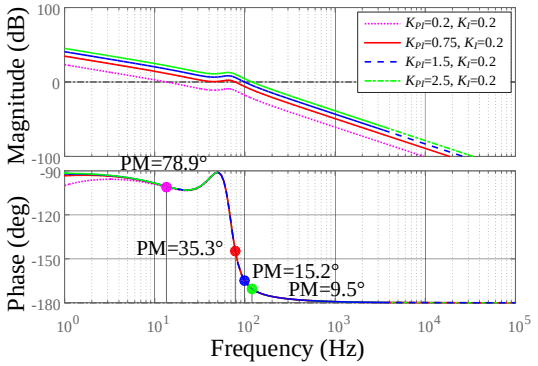

Fig. 9. Bode diagram with varying K_{PI} in voltage loop.

$$G_{i\_op}(s) = K_{PWM} \cdot G_{PR}(s) \cdot G_d(s) \frac{1}{Ls} \tag{18}$$

where the K_{PWM} is the PWM coefficient, and the G_d(s) is the system delay, which includes one sampling period T_s and another delay $0.5T_s$ introduced by the modulator. The total delay in the control loop is, thus, $1.5T_s$, expressed exponentially as:

$$G_d(s) = e^{-1.5T_s s}. \tag{19}$$

According to the $G_{i\_op}(s)$, we can obtain the stability analysis of the inner loop. The bode diagram of the open-loop system can be plotted in Fig. 8. The gain margin (GM) and phase margin (PM) are all larger than 0 with the given parameters. Thus, the system is theoretically stable. Considering the parameters have some deviation from the theoretical values, the PM is selected between 30° and 60° in this paper. Fig. 8(a) shows the PM under varying K_{PR} and fixed K_R. When the K_{PR} is equal to 2, the PM is equal to 49°, and the other values of K_{PR} make the PM larger than 60°. Similarly, when the K_R is equal to 50 or 100 in Fig. 8 (b), the PM is within 30° to 60°. But the magnitude gain is larger when the K_R is equal to 100. Thus, the K_{PR} and K_R are selected as 2 and 100, respectively.

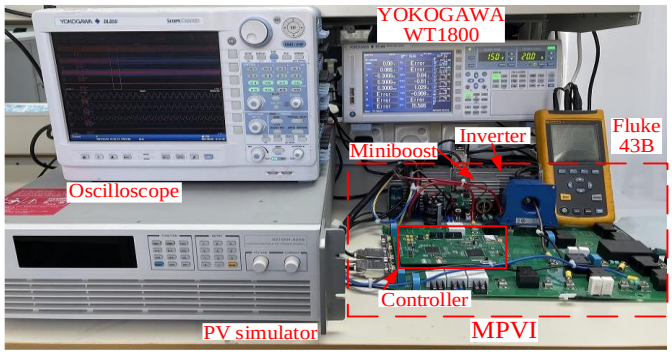

Fig. 10. Experimental setup of the 1.5kVA single-phase prototype.

TABLE III
EXPERIMENTAL SETUP PARAMETERS

Description		Parameters	Values
Source	Voltage (rms)	V_s	115V
	Frequency	f_1	50Hz
Load	Load1	Q_L	1.1kVar
	Load2	THD	45.7%
Proposed MPVI	Coupling inductor	L	5mH
	Inverter rating	S_N	1.5kVA
	Boost inductor	L_B	2mH
	Miniboost rating	S_{dc}	1kW
	Switching frequency	f_{sw}	15kHz

According to the outer voltage loop of the inverter controller in Fig. 7, the transfer function of the voltage loop is given in (20).

$$G_{v\_op}(s) = G_{PI}(s) \cdot \frac{G_{i\_op}(s)}{1 + G_{i\_op}(s)} \cdot \frac{1}{C_{dc} \cdot s} \tag{20}$$

Based on the above analysis for the inner current loop, the K_{PR} and K_R are 2 and 100, respectively. Accordingly, the bode diagram of the voltage loop plots in Fig. 9. The system is stable under the given parameters, and the PM is appropriate between 30° and 60° when K_{PI} and K_I are equal to 0.75 and 0.2, respectively. Thus, the K_{PI} and K_I are selected as 0.75 and 0.2, respectively.

V. EXPERIMENTAL RESULTS AND DISCUSSIONS

A single-phase 1.5kVA experimental prototype is designed and constructed in the laboratory, as shown in Fig. 10. The controller of the prototype consists of a digital signal processor (DSP) TMS320F28335 and a field-programmable gate array (FPGA) 10M02SCE144I7G. The PV simulator model is 62100H-600S produced by CHROMA. The THD is measured by Fluke 43B, and the power data is measured by YOKOGAWA WT1800. All the experimental waveforms are recorded by oscilloscope YOKOGAWA DL850.

To avoid beat frequency oscillation that occurs in two or more interconnected power converters [23], [24], two ways are adopted to eliminate the beat frequency oscillation in the experiment. Namely, on the one hand, the switching frequencies of the miniboost and H-bridge inverter are set to be the same to eliminate the beat switching frequency component. On the other hand, a larger capacitor paralleled with miniboost output can dampen the voltage ripple. Thus, even if there is a low beat

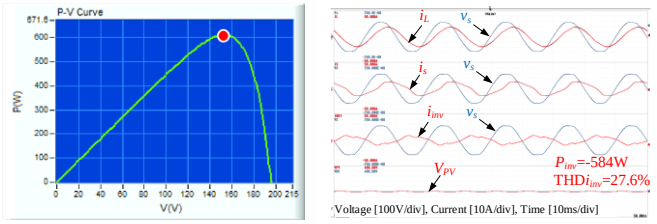

(a) (b)

Fig. 11. (a) MPPT performance and (b) experimental v_s, i_L, i_s, V_{PV} waveforms in the condition of V_{PV}=V_{MPP} in single-stage PV-connected PG mode.

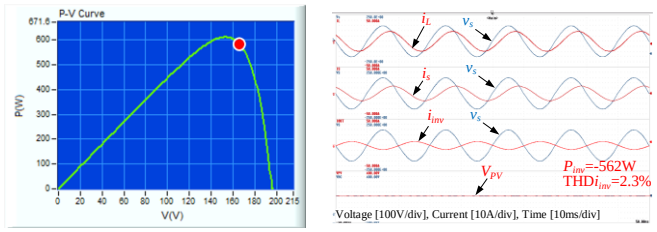

(a) (b)

Fig. 12. (a) MPPT performance and (b) experimental v_s, i_L, i_s, V_{PV} waveforms in the condition of V_{PV}>V_{MPP} in single-stage PV-connected PG mode.

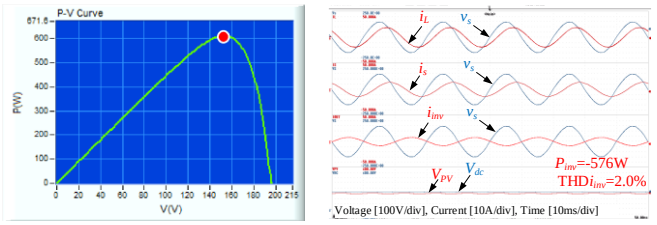

(a) (b)

Fig. 13. (a) MPPT performance and (b) experimental v_s, i_L, i_s, V_{PV} waveforms in the condition of V_{PV}=V_{MPP} in two-stage PG mode.

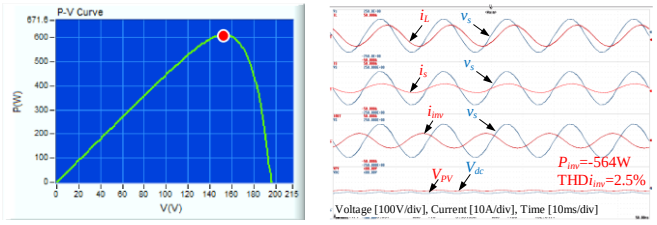

(a) (b)

Fig. 14. (a) MPPT performance and (b) experimental v_s, i_L, i_s, V_{PV} waveforms in the condition of V_{PV}=V_{MPP} in two-stage MF mode.

TABLE IV
SUMMARY OF LOW MPP VOLTAGE OPERATION DATA

	(V_{MPP}, P_{MPP})	V_{PV} (V)	MPP	V_{dc} (V)	P_{inv} (W)	Q_{inv} (Var)	η	THDi_{inv} (%)	PF_s
Fig. 11	(152,610)	152	☑	152	584	32	0.957	27.6	0.52
Fig. 12	(152,610)	165	☒	165	562	26	0.921	2.3	0.52
Fig. 13	(152,610)	152	☑	165	576	34	0.944	2.0	0.52
Fig. 14	(152,610)	152	☑	177	564	950	0.925	2.5	1.0

frequency, the beat frequency is shifted to a high frequency to avoid amplifying by high gains of the inverter controller.

The experimental parameters are given in TABLE III. In this section, varying P-V conditions are taken as discussed in section III to verify:

1) the correctness and feasibility of graphical analysis between phasor and PV curve;

2) the problems of harmonic emission, low efficiency, and weak compensation capability can be solved by the proposed MPVI to transfer different operation modes adaptively based on the operational criteria;

3) dynamic performance of the proposed MPVI.

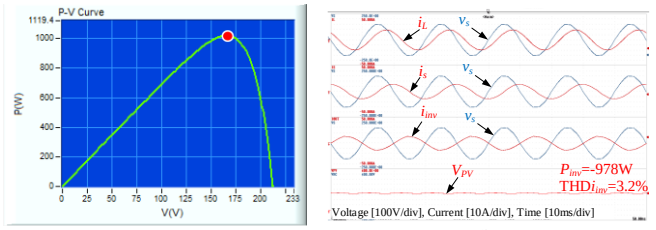

(a) (b)

Fig. 15. (a) MPPT performance and (b) experimental v_s, i_L, i_s, V_{PV} waveforms in the condition of V_{PV}=V_{MPP} in single-stage PV-connected PG mode.

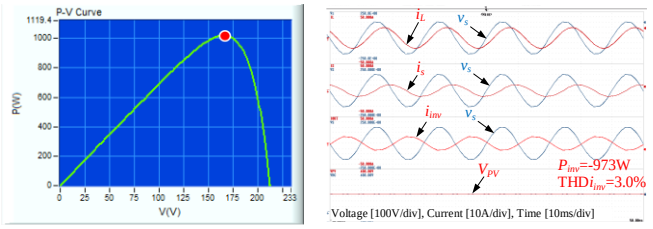

(a) (b)

Fig. 16. (a) MPPT performance and (b) experimental v_s, i_L, i_s, V_{PV} waveforms in the condition of V_{PV}=V_{MPP} in single-stage PV-connected MF mode.

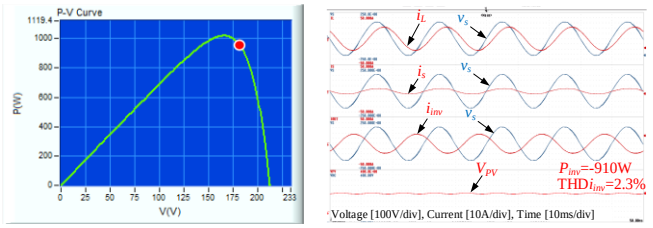

(a) (b)

Fig. 17 (a) MPPT performance and (b) experimental v_s, i_L, i_s, V_{PV} waveforms in the condition of V_{PV}>V_{MPP} in single-stage PV-connected MF mode.

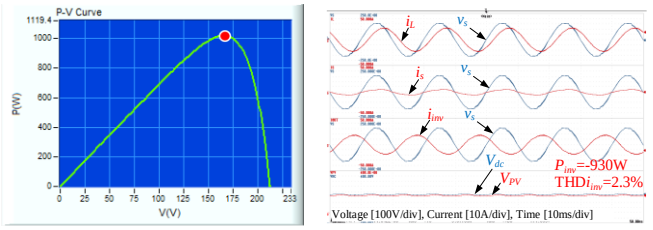

(a) (b)

Fig. 18. (a) MPPT performance and (b) experimental v_s, i_L, i_s, V_{PV} waveforms in the condition of V_{PV}=V_{MPP} in two-stage MF mode.

TABLE V
SUMMARY OF MARGINAL MPP VOLTAGE OPERATION DATA

	(V_{MPP}, P_{MPP})	V_{PV} (V)	MPP	V_{dc} (V)	P_{inv} (W)	Q_{inv} (Var)	η	THDi_{inv} (%)	PF_s
Fig. 15	(165,1017)	165	☑	165	978	10	0.962	2.2	0.18
Fig. 16	(165,1017)	165	☑	165	973	160	0.957	3.0	0.24
Fig. 17	(165,1017)	181	☒	181	910	1124	0.895	2.3	1.0
Fig. 18	(165,1017)	165	☑	181	930	1091	0.914	2.3	1.0

A. Low MPP Voltage

In this part, the MPP (152V, 610W) is similar to MPP_3 in section III. Fig. 11 and Fig. 12 use single-stage PV-connected mode to illustrate the undesired harmonic emission. The source voltage magnitude is 162V (115V rms) is larger than the MPP voltage (152V). The MPP operation is achieved as shown in Fig. 11(a). Fig. 11(b) shows that the THD of the inverter current is 27.6%. In Fig. 12, the dc voltage is increased to V_{PGdc} (165V). The inverter operates without MPP but the undesired harmonic current is suppressed. The proposed MPVI operates in the two-

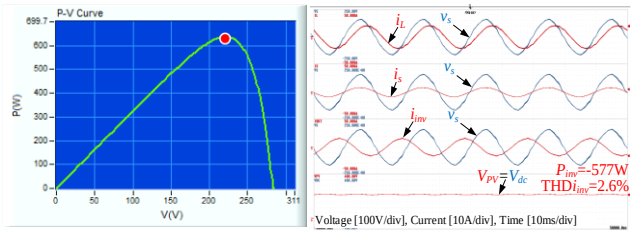

(a) (b)

Fig. 19. (a) MPPT performance and (b) Experimental v_s, i_L, i_s, V_{PV}, V_{dc} waveforms of the proposed MPVI operate in two-stage mode when MPP voltage is relatively high.

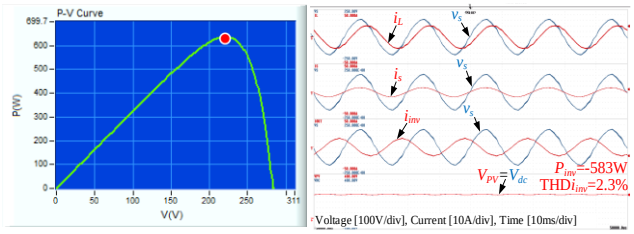

(a) (b)

Fig. 20. (a) MPPT performance and (b) Experimental v_s, i_L, i_s, V_{PV}, V_{dc} waveforms of the proposed MPVI in single-stage PV-connected mode when MPP voltage is relatively high.

TABLE VI
SUMMARY OF HIGH MPP VOLTAGE OPERATION DATA

	(V_{MPP}, P_{MPP})	V_{PV} (V)	MPP	V_{dc} (V)	P_{inv} (W)	Q_{inv} (Var)	η	THDi_{inv} (%)	PF_s
Fig. 19	(220,636)	220	☑	220	577	1035	0.907	2.6	1.0
Fig. 20	(220,636)	220	☑	220	583	1026	0.917	2.3	1.0

stage mode, as shown in Fig. 13. Compared with Fig. 12, the THD of the inverter current is similar, and the efficiency is improved by 2.5%.

The required dc voltage of the inverter in the MF mode is larger than that of the PG mode (V_{FCdc}>V_{PGdc}) when other conditions are unchanged. The dc voltage is regulated to 177V for full compensation, as shown in Fig. 14. The experiment data is summarized in TABLE IV.

B. *Marginal MPP Voltage*

In this part, the MPP (165V, 1017W) is similar to MPP_1 in section III. The inverter can inject maximum power injection at marginal MPP voltage, as shown in Fig. 15, in which the injected current is not distorted. If reactive power compensation is performed, the required dc voltage becomes larger than the MPP voltage. Only partial compensation can be performed to avoid harmonic emission, as shown in Fig. 16. The inverter injects 160Var reactive power with MPP operation. But the source power factor is only 0.24 after compensation. When the PV voltage is regulated to V_{FCdc}, the inverter can compensate all reactive current without MPP operation as shown in Fig. 17.

The proposed MPVI operates in the two-stage mode as shown in Fig. 18. The reactive power is fully compensated with MPP operation. Compared with Fig. 17, the efficiency is increased by 2.1%. The experiment data is summarized in TABLE V, in which the two-stage mode is preferred with high power quality injected current and full compensation.

C. *High MPP Voltage*

In this part, the MPP (220V, 636W) is similar to MPP_2 in section III. Fig. 19 and Fig. 20 show the waveforms of the proposed MPVI operating in two-stage mode (B_B OFF) and single-stage PV-connected mode (B_B ON), respectively. The two experimental waveforms are very similar. The injected active power into the grid is different as shown in TABLE VI since the solar energy flows through the miniboost, causing larger operational losses (P_{MPP}-P_{inv}) in the two-stage mode. Under this situation, the single-stage PV-connected mode is preferred with higher efficiency (1.1%) since the solar energy flows through the B_B instead of the miniboost.

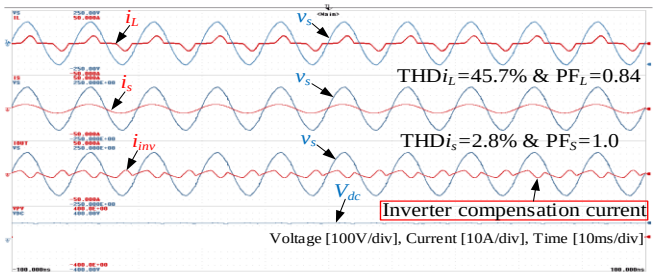

Fig. 21. Experimental v_s, i_L, i_s, V_{PV}, V_{dc} waveforms of the proposed MPVI in compensation mode.

D. *Compensation Mode*

In Fig. 21, the proposed MPVI is operated in compensation mode. The reactive power and harmonic currents can be compensated by the proposed MPVI. The injection reactive power is 160 Var. The PF_S and THDi_S are improved to 1.0 and 2.8% after compensation, respectively.

E. *Dynamic Performance Verification*

To verify the feasibility of the proposed control strategy, the dynamic experiments between single-stage PV-connected mode and two-stage mode under varying load conditions are shown in Fig. 22 and Fig. 23. In Fig. 22, the reactive power of the load becomes larger. As a result, the V_{FCdc} becomes larger than V_{MPP}. The proposed MPVI transfers from single-stage PV-connected operation mode to two-stage operation mode to perform full compensation. In Fig. 23, the reactive power of the load becomes smaller. As a result, the V_{FCdc} becomes less than V_{MPP}. The proposed MPVI transfers from the two-stage operation mode to the single-stage PV-connected operation mode to improve the system efficiency. Experimental results show that the transfer process is smooth, and the switching time is relatively short. They verify the feasibility and effectiveness of the proposed control strategy.

VI. CONCLUSION

The harmonic emission puzzle and weak compensation capability are exposed by the proposed graphical analysis under varying PV conditions. When the inverter operates at MPP and the corresponding MPP voltage is low, the inverter easily falls into the overmodulation region. As a result, harmonic emission occurs. Reducing the reactive power output can alleviate the overmodulation region, but the compensation capability becomes weak. Thus, a time-sharing miniboost MPVI with single-stage PV-connected mode, single-stage alone mode, and two-stage mode is proposed. The proposed MPVI transfer among these operation modes adaptively based on the operational criteria to address undesired harmonic emission and weak compensation capability. The corresponding control

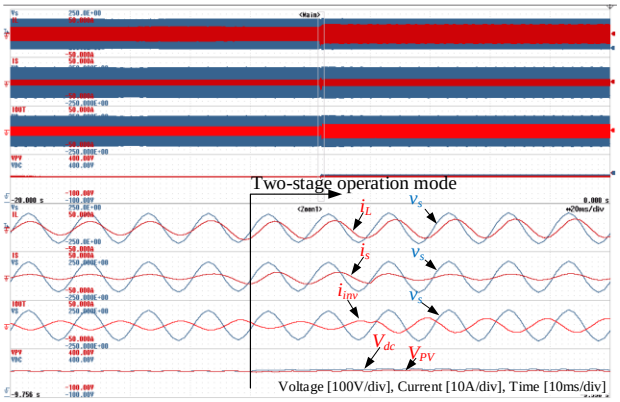

Fig. 22. Transition from single-stage PV-connected operation mode to two-stage operation mode of the proposed MPVI in the experiment.

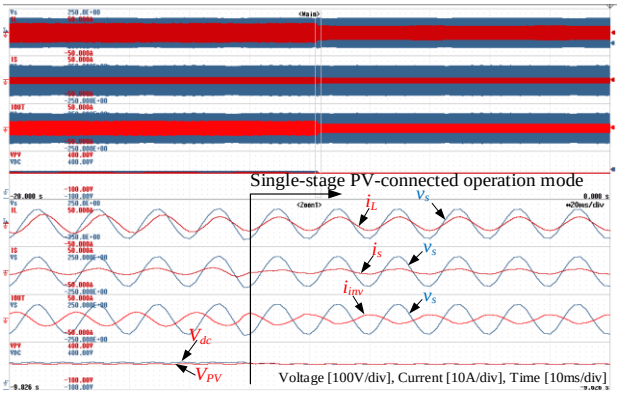

Fig. 23. Transition from two-stage operation mode to single-stage PV-connected operation mode of the proposed MPVI in the experiment.

strategy and stability analysis are given and verified by experimental results. Compared to the method without the proposed operational criteria, the results show that the proposed approach can perform MPP operation and full compensation simultaneously, especially the undesired harmonics is eliminated (THD ≤ 2.5%) and the efficiency is improved by 1.1~2.5%.

REFERENCES

[1] J. H. Yi, R. Cherkaoui and M. Paolone, "Optimal Allocation of ESSs in Active Distribution Networks to Achieve Their Dispatchability," *IEEE Trans. Power Syst*., vol. 36, no. 3, pp. 2068-2081, May 2021.

[2] M. N. H. Khan, M. Forouzesh, Y. P. Siwakoti, L. Li, T. Kerekes and F. Blaabjerg, "Transformerless Inverter Topologies for Single-Phase Photovoltaic Systems: A Comparative Review," *IEEE J. Emerg. Sel. Topics Power Electron.*, vol. 8, no. 1, pp. 805-835, Mar. 2020.

[3] E. Koutroulis and F. Blaabjerg, "A New Technique for Tracking the Global Maximum Power Point of PV Arrays Operating Under Partial-Shading Conditions," *IEEE J. Photovolt.*, vol. 2, no. 2, pp. 184-190, Apr. 2012.

[4] A. Sangwongwanich and F. Blaabjerg, "Mitigation of Interharmonics in PV Systems With Maximum Power Point Tracking Modification," *IEEE Trans. Power Electron*., vol. 34, no. 9, pp. 8279-8282, Sep. 2019.

[5] K. K. Prasad, H. Myneni and G. S. Kumar, "Power Quality Improvement and PV Power Injection by DSTATCOM With Variable DC Link Voltage Control from RSC-MLC," *IEEE Trans. Sustain. Energy*, vol. 10, no. 2, pp. 876-885, Apr. 2019.

[6] L. S. Xavier, A. F. Cupertino, H. A. Pereira and V. F. Mendes, "Partial Harmonic Current Compensation for Multifunctional Photovoltaic Inverters," *IEEE Trans. Power Electron*., vol. 34, no. 12, pp. 11868-11879, Dec. 2019.

[7] V. Ravindran, T. Busatto, S. K. Rönnberg, J. Meyer and M. H. J. Bollen, "Time-Varying Interharmonics in Different Types of Grid-Tied PV Inverter Systems," *IEEE Trans. Power Delivery*, vol. 35, no. 2, pp. 483-496, Apr. 2020.

[8] D. Meneses, F. Blaabjerg, Ó. García and J. A. Cobos, "Review and Comparison of Step-Up Transformerless Topologies for Photovoltaic AC-Module Application," *IEEE Trans. Power Electron*., vol. 28, no. 6, pp. 2649-2663, Jun. 2013.

[9] T. V. Thang, N. M. Thao, J. Jang and J. Park, "Analysis and Design of Grid-Connected Photovoltaic Systems With Multiple-Integrated Converters and a Pseudo-DC-Link Inverter," *IEEE Trans. Ind. Electron*., vol. 61, no. 7, pp. 3377-3386, Jul. 2014.

[10] A. Anurag, N. Deshmukh, A. Maguluri and S. Anand, "Integrated DC–DC Converter Based Grid-Connected Transformerless Photovoltaic Inverter With Extended Input Voltage Range," *IEEE Trans. Power Electron*., vol. 33, no. 10, pp. 8322-8330, Oct. 2018.

[11] J.Wang, H.Wu, T. Yang, L. Zhang, and Y. Xing, "Bidirectional three-phase DC–AC converter with embedded DC–DC converter and carrier-based PWM strategy for wide voltage range applications," *IEEE Trans. Ind. Electron.*, vol. 66, no. 6, pp. 4144–4155, Jun. 2019.

[12] J. Wang, K. Sun, H. Wu, L. Zhang, J. Zhu and Y. Xing, "Quasi-Two-Stage Multifunctional Photovoltaic Inverter With Power Quality Control and Enhanced Conversion Efficiency," *IEEE Trans. Power Electron*., vol. 35, no. 7, pp. 7073-7085, Jul. 2020.

[13] K. Ogura, T. Nishida, E. Hiraki, M. Nakaoka and S. Nagai, "Time-sharing boost chopper cascaded dual mode single-phase sinewave inverter for solar photovoltaic power generation system," *Proc. IEEE Power Electron. Spec. Conf.*, pp. 4763-4767, 2004.

[14] E. Serban, F. Paz and M. Ordonez, "Improved PV Inverter Operating Range Using a Miniboost," *IEEE Trans. Power Electron*., vol. 32, no. 11, pp. 8470-8485, Nov. 2017.

[15] H. Li, D. Yang, W. Su, J. Lü, and X. Yu, "An overall distribution particle swarm optimization MPPT algorithm for photovoltaic system under partial shading," *IEEE Trans. Ind. Electron.*, vol. 66, no. 1, pp. 265–275, Jan. 2019.

[16] J. Jeong, M. Shim, J. Maeng, I. Park and C. Kim, "A High-Efficiency Charger With Adaptive Input Ripple MPPT for Low-Power Thermoelectric Energy Harvesting Achieving 21% Efficiency Improvement," *IEEE Trans. Power Electron*., vol. 35, no. 1, pp. 347-358, Jan. 2020.

[17] T. Wu, C. Chang, L. Lin and C. Kuo, "Power Loss Comparison of Single- and Two-Stage Grid-Connected Photovoltaic Systems," *IEEE Trans. Energy Convers*., vol. 26, no. 2, pp. 707-715, Jun. 2011.

[18] S.K. Khadem, M. Basu and M.F. Conlon, "Harmonic power compensation capacity of shunt active power filter and its relationship with design parameters," *IET Power Electron*., Vol. 7, no. 2, pp. 418–430, Feb. 2014.

[19] C. Zhou, G. Yang and J. Su, "PWM Strategy With Minimum Harmonic Distortion for Dual Three-Phase Permanent-Magnet Synchronous Motor Drives Operating in the Overmodulation Region," *IEEE Trans. Power Electron*., vol. 31, no. 2, pp. 1367-1380, Feb. 2016.

[20] A. Luo, Y. Chen, Z. Shuai and C. Tu, "An Improved Reactive Current Detection and Power Control Method for Single-Phase Photovoltaic Grid-Connected DG System," *IEEE Trans. Energy Convers*., vol. 28, no. 4, pp. 823-831, Dec. 2013.

[21] D. Kanavaros, G. Oriti and A. L. Julian, "Novel Implementation and Comparison of Active and Reactive Power Flow Control Methods in a Single Phase Grid-Connected Microgrid," *IEEE Trans. Ind. Appl.*, vol. 56, no. 2, pp. 1631-1639, Mar.-Apr. 2020.

[22] K. Chen, S. Tian, Y. Cheng and L. Bai, "An Improved MPPT Controller for Photovoltaic System Under Partial Shading Condition," *IEEE Trans. Sustain. Energy*, vol. 5, no. 3, pp. 978-985, Jul. 2014.

[23] K. Li, S. -C. Tan and R. S. Y. Hui, "On Beat Frequency Oscillation of Two-Stage Wireless Power Receivers," *IEEE Trans. Power Electron*., vol. 35, no. 12, pp. 12741-12751, Dec. 2020.

[24] X. Yue, F. Zhuo, S. Yang, Y. Pei and H. Yi, "A Matrix-Based Multifrequency Output Impedance Model for Beat Frequency Oscillation Analysis in Distributed Power Systems," *IEEE J. Emerg. Sel. Topics Power Electron*., vol. 4, no. 1, pp. 80-92, Mar. 2016.

Zeng Xiang (Member, IEEE) received the B.Sc. degree in Electrical Engineering and Automation from Tianjin University of Science & Technology, in 2009, Tianjin, China. He received his M.Sc. degree in Electronic Engineering from Hunan University, in 2012, Changsha, China.
He is currently working toward the Ph.D. degree in Electrical and computer engineering with State Key Laboratory of Internet of Things for Smart City, University of Macau, Macau.

Ying Pang (Student Member, IEEE) received the B.Sc. degree in electrical engineering from Southwest Jiaotong University, Chengdu, China, in 2015, and the M.Sc. degree in electrical and computer engineering from the University of Macau, Macao SAR, China, in 2018, where he is currently pursuing the Ph.D. degree in electrical and computer engineering with the State Key Laboratory of Internet of Things for Smart City. His research interests include power filter, smart grid, renewable energy, and distributed generation.

Ziyi Bai received the B.Sc. degree in electrical engineering from Hainan University, Haikou, China, in 2016, and the M.Sc. degree in electrical engineering from Hunan University, Changsha, China, in 2019. She is currently working toward the Ph.D. degree in Electrical and computer engineering with State Key Laboratory of Internet of Things for Smart City, University of Macau, Macau. Her research interests include power filter, renewable energy, and distributed generation.

Lei Wang (Senior Member, IEEE) received the B.Sc. degree in Electrical and Electronics Engineering from University of Macau (UM), Macao SAR, P. R. China, in 2011, M.Sc. degree in Electronics Engineering from Hong Kong University of Science and Technology (HKUST), Hong Kong SAR, P. R. China, in 2012. and Ph.D. degree in Electrical and Computer Engineering from University of Macau (UM), Macao SAR, P. R. China, in 2017. He was a postdoctoral fellow in the Power Electronics Laboratory of UM from Jan. 2017 to Feb. 2019. In 2019, he joined College of Electrical and Information Engineering, Hunan University, Changsha, China, where he is currently a Full Professor.

Chi-Kong Wong (Member, IEEE) received the B.Sc. and M.Sc. degrees in electrical and electronics engineering from the University of Macau (UM), Macao, China, in 1993 and 1997, respectively, and the Ph.D. degree in electrical engineering from Tsinghua University, Beijing, China, in 2007.
Since 1993, he has been a Teaching Assistant with the Faculty of Science and Technology, UM, where he was promoted as a Lecturer and an Assistant Professor in 1997 and 2008, respectively.

Wai-Hei Choi (Member, IEEE) received the B.Sc. and M.Sc. degrees in electrical and electronics engineering from the University of Macau (UM), Macao, China, in 2009 and 2012, respectively, where he is currently pursuing the Ph.D. degree. From 2012 to 2014, he was a Research Assistant with the Power Electronics Laboratory, UM, where he is currently a Technician with the Electric Power Engineering Laboratory.

Chi-Seng Lam (Senior Member, IEEE) received the Ph.D. degree in electrical and electronics engineering from the University of Macau (UM), Macao, China, in 2012. He completed the Clare Hall Study Program at the University of Cambridge, Cambridge, U.K., in 2019.
He is currently an Associate Professor with the State Key Laboratory of Analog and Mixed-Signal VLSI and the Institute of Microelectronics, UM, and also with the Department of Electrical and Computer Engineering, Faculty of Science and Technology, UM.

Man-Chung Wong (Senior Member, IEEE) received the B.Sc. and M.Sc. degrees in Electrical and Electronics Engineering from University of Macau (UM), Macao, China, in 1993 and 1997, respectively; and received his Ph.D. degree in Electrical Engineering from Tsinghua University, Beijing, P. R. China, in 2003.
Currently, he is a professor in the Department of Electrical and Computer Engineering, University of Macau.